

# Numerical Generation of Double Star Images for Different Types of Telescopes

Ademir Xavier

DTR - Division of Network Technologies, Renato Archer Center for Technology  
Information CEP 13069-901, Campinas, SP, Brazil  
[xavnet2@gmail.com](mailto:xavnet2@gmail.com)

**Abstract:** This paper reviews the modeling of stellar images using diffraction theory applied to different types of telescope masks. The masks are projected by secondary mirror holder vanes (such as the spider type) or holes on the primary mirror which result in different configurations of single stellar images. Using Fast Fourier Transform, the image of binary stars with different magnitudes is calculated. Given the numerical results obtained, a discussion is presented on the best secondary vane configurations and on the effect of obstruction types for the separation of binary pairs with different magnitudes.

## Introduction

Since the invention of the telescope, the use of high magnification was soon recognized as a good technique to access the telescope's optical quality. The test can include the observation of close binary stars which, depending on their apparent separation, is also a measure of the telescope's resolving power. However, the evaluation should be performed under pristine atmospheric conditions, which are rarely found at most locations.

The process of image formation in telescopes [Schroeder 1987] is complementarily described by two distinct approaches: i) light rays' propagation from a distant object, reflection and refraction at different optical surfaces and/or media and image formation at primary focus; ii) incident wave fronts from the distant object that is reflected and/or refracted, suffering diffraction at optical apertures. The latter approach is based on the famous wave-particle duality of light. Nonetheless, in this article, the geometric (particle) part of image formation will not be considered. Instead, our aim is to review a succinct way of numerically determining stellar images using only the diffractive (wavelike) description of light entering the telescope tube. According to this model, the telescope is represented exclusively by its aperture, considered as an optical mask on which obstacles are projected. These arrangements are as assorted as the various secondary mirror holder types that exist in reflection telescopes or holes in primary mirrors, as in the case of Schmidt-

Cassegrain, Schmidt-Newtonian, Maksutov-Cassegrain, to quote a few. Then, the model can be used to predict double star images close to Dawes' limit [Argyle 2004] having different magnitude components.

The phenomena of companion disappearance in the presence of diffraction rings around a primary star can be entirely simulated. The effort is in line with the search for new methodologies for predicting images in amateur telescopes [Napier-Munn 2008, Berrevoets 2001] and simulation software for optical testing. We therefore review the diffraction theory in the first section and numerically integrate the Fresnel-Kirchhoff equation for several telescope masks in the following sections. The numerical procedure is applied to masks that substantially deviate from the simple circular aperture used as a standard pattern in terms of which limiting magnitudes for a companion are extracted as a function of the separation from the main star. This approach somewhat justifies the excellence of refractors as instruments for double star observation at the same time that it provides some guiding to align the telescope in order to enhance the contrast between each component depending on the telescope mask.

## Diffraction theory

Light coming from a distance source like a star is described as a continuous flow of wavelike radiation that enters the telescope. Wave fronts are reflected or refracted by the several telescope optical elements with the major component (the refractor objective or reflec-

## Numerical Generation of Double Star Images for Different Types of Telescopes

tor primary mirror) acting as an aperture stop where light is diffracted. Diffraction is the main cause for a star image to never show any detail of its surface. To minimize diffraction effects (and therefore obtain detailed images), large primaries are constructed with the additional benefit of increasing the amount of collected light. Wave fronts at the aperture can be represented as oscillations in a local incident electric field  $E_{inc}(\mathbf{r}_A)$ , where  $\mathbf{r}_A$  is the aperture coordinate in a predefined coordinate system. According to the Fresnel-Kirchhoff formulation of Huygens' Principle (Klein, 1970), the electric field at a point  $\mathbf{r}$  beyond the aperture will be given by

$$E(\mathbf{r}) = \frac{i}{\lambda} \iint H(\mathbf{r}_A) E(\mathbf{r}_A) \frac{e^{-ik|\mathbf{r}-\mathbf{r}_A|}}{|\mathbf{r}-\mathbf{r}_A|} d\sigma_A \quad (1)$$

where  $\lambda$  is the light wavelength (assumed monochromatic),  $k = 2\pi/\lambda$ ,  $d\sigma_A$  is a differential element of area (on the aperture), and  $H(\mathbf{r}_A)$  is the aperture stop function. The value of  $\lambda$  can be taken as the wavelength of yellow light (570 - 590 nm) to better approximate the eye's maximum sensitivity (Barten, 1999). Eq. (1) is the mathematical formulation of all contributions coming from the aperture at the point of interest ( $\mathbf{r}$ ) which can be taken as the telescope focus. Another important comment about the application of Eq. (1) to reality is that it represents the contribution of a single frequency component of non-polarized light. The output field of Eq. (1) is polarized in accordance with the incident amplitude  $E(\mathbf{r}_A)$ . Therefore, Eq. (1) works as a *scalar model* for light diffraction.

The next step is to take a linear approximation for the path differences of the several contributions of diffracted fields. For point-like objects like stars – in which case the direction cosines of a target object at the primal focus are very small – the approximation is sufficient to render a finished simulated image. Eq. (1) can be transformed to

$$E(\mathbf{r}) = \frac{i}{\lambda} E_A \iint H(x_A, y_A) e^{-ik(\alpha x_A + \beta y_A)} dx_A dy_A \quad (2)$$

Here  $E_A$  is a phase factor proportional to the light intensity at the aperture and  $\alpha$  and  $\beta$  are the position angles of the source. Therefore, the image intensity at the telescope focus can be modelled as the space Fourier transform of the aperture  $(x_A, y_A)$  having the pair  $(\alpha, \beta)$  as conjugate variables. The classical example is the circular aperture with diameter  $D$  of a (refractor) telescope for which the resulting field at focus  $f_0$  can be expressed by the closed function



Figure 1. Maksutov-Cassegrain telescope showing its aperture mask.

$$E(\alpha) = E_A \frac{e^{ikf_0}}{2f_0} iD \frac{J_1[k(D/2)\sin\alpha]}{\sin\alpha} \quad (3)$$

with  $J_1(p)$  the first order Bessel function of argument  $p$ , whose first zero is at  $1.22\pi$ , resulting in the Airy's disk radius. Therefore, the resolving power (in radians) of the instrument will be given by

$$r_p = \frac{1.22\lambda}{D} \quad (4)$$

since the minimum separation possible corresponds to the radius of the diffraction disk. Once the total received power is proportional to the square of the electric field, Eq. (3) also predicts that light intensity at the focus is inversely proportional to the square of the  $f_0/D$  ratio

### Numerical Integration of Fresnel-Kirchhoff Integral

Except for the somewhat artificial case of a squared aperture (Klein, 1970), other cases can only be analyzed by numerical simulation of Eq. (2). Let us denote  $u = x_A$  and  $v = y_A$  the coordinates on the aperture planes. If  $\Theta(x)$  represents Heaviside's function (Abramowitz & Stegun, 1972) such that  $\Theta(x) = 1$  for  $x > 0$ , and  $\Theta(x) = 0$  otherwise, an aperture stop described by a main radius of  $R_1$  and a small hole of radius  $R_2$  ( $R_2 < R_1$ ) may be represented by the two parameter function:

$$H_{hole}(u, v) = \Theta\left(R_1 - \sqrt{u^2 + v^2}\right) \Theta\left(\sqrt{u^2 + v^2} - R_2\right) \quad (5)$$

A refractor aperture case can be simulated using Eq. (5) in (2) and making  $R_2 = 0$ . On the other hand, a Maksutov-

Numerical Generation of Double Star Images for Different Types of Telescopes

Cassegrain mask (Figure 1) is simulated with Eq. (5) and a finite  $R_2$ . A simple secondary holder vane can be added to Eq. (5) with the function

$$H_{sh}(u,v) = \Theta \left[ \Theta \left( \left| v - \frac{w}{2} \right| + \Theta(u-l) + \Theta(-u) \right) \right] \quad (6)$$

where  $w$  and  $l$  are the holder width and length respectively. A complete simple secondary holder will be the product of Eq. (5) and Eq. (6). To simulate a spider vane, we consider the rotated version of Eq. (6)

$$H\phi(u,v) = \Theta \left[ \Theta \left( \left| v \cos \phi - u \sin \phi - \frac{w}{2} \right| + \Theta(u \cos \phi + v \sin \phi - l) + \Theta(-u \cos \phi - v \sin \phi) \right) \right] \quad (7)$$

with  $\phi$  the rotation angle. A spider mask will then be represented by the following function:

$$H_{spider}(u,v) = H_{hole}(u,v) H_{\frac{2\pi}{3}}(u,v) H_{\frac{2\pi}{3}}(u,v) H_{sh}(u,v) \quad (8)$$

Figure 2 is a contour plot representation of several aperture masks as a binary map generated on a 1024 x 1024 grid in an enclosure space with side  $L = 2$ ,  $R_1 = 0.5$  and  $R_2 = \epsilon R_1$  and  $\epsilon = 0.15$ . Here, units are arbitrary and do not represent any specific measure. In order to reproduced the image of a single star, we apply Eq. (2), which involves the application of a fast Fourier transformation (FFT) (Cooley, Lewis, & Welch, 1967) of the aperture

$$S(\alpha, \beta) = \text{FFT} [ H(u,v) ] \quad (9)$$

Here  $(\alpha, \beta)$  are conjugate coordinates in the transformed space. For all practical purposes,  $|S(\alpha, \beta)|^2$  is proportional to the image intensity. Also, the  $(a,b)$  pair is mapped by the indexes of the output FFT matrix  $(i,j)$ . In order to apply the FFT and generate a star image, we use the function `fft()` of MATHCAD (PTC, 2010) which requires the output to be recombined in order to build the final image. For simplicity, we will not describe these operational details here. As an example, the output of Eq. (2) for a refractor mask, Eq. (5), is shown in Figure 3. The simulation parameters are  $L = 1.4$ , and  $R_1 = 0.3$  and the input grid has 1024 X 1024 points.

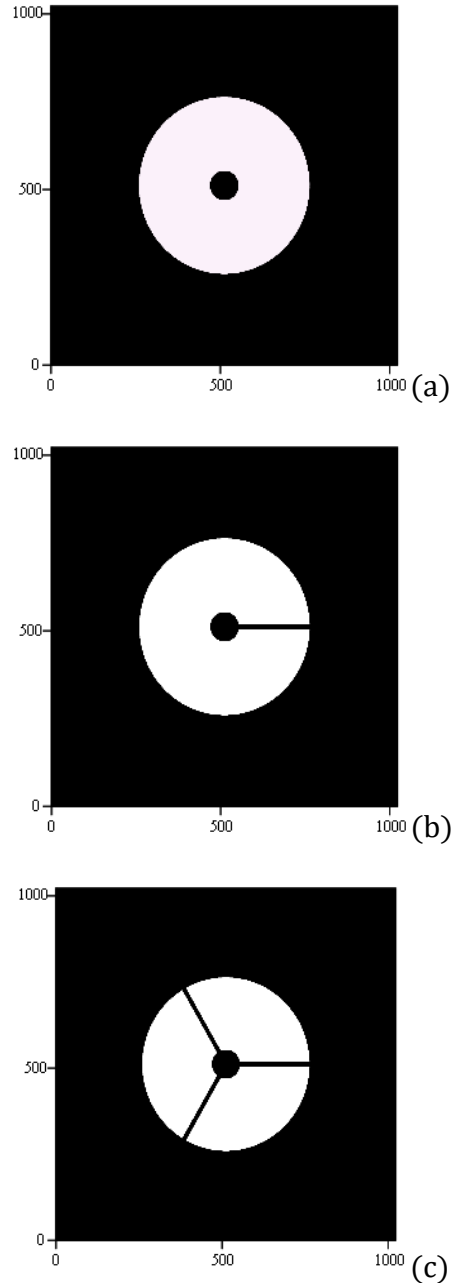
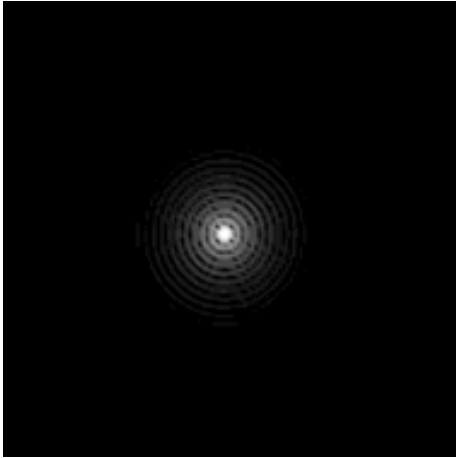


Figure 2. Possible telescope mask functions on the  $(u,v)$  plane generated with a 1024 X1024 input grid. (a) Circular hole (Eq. 5); (b) single holder vane, Eq. (6); (c) spider vane or Eq. (8). The  $(u,v)$  plane is within a box with  $L = 2$ . In (a),  $R_1 = 0.5$ ,  $R_2 = 0.075$  ( $\epsilon = 0.15$ ). In (b) and (c),  $w = 0.01$  and  $l = 0.5$ , see Eq. (7) and (8).

### Numerical Generation of Double Star Images for Different Types of Telescopes



*Figure 3. Simulated star (Eq. 10) with 235 X 235 points for a refractor mask ( $R_1=0$ ) and  $\varepsilon=1$ .*

The image in Figure 3 is a contour plot in grey scale of the intensity function

$$I(\alpha, \beta) = \log\left(|S(\alpha, \beta)|^2 + \varepsilon\right) \quad (10)$$

with  $\varepsilon$  a constant factor and  $\log$  is the logarithm to base 10. The smaller  $\varepsilon$  the more defined are the diffraction rings or, in other words, as  $\varepsilon$  increases ring contrast reduces. In fact,  $\varepsilon$  can be thought of as a sky background factor, which should be substituted by a stochastic amplitude variation function representing atmospheric turbulence for realistic purposes. Therefore, the image of Figure 3 only in its first rings resembles a real star image.

Using the same parameter inputs of Figure 3, it is possible to simulate star images for the telescope masks of Figure 2. These are presented in Figure 4. Each frame in this image corresponds to the masks of Figure 2 in respective order. As one can see, the effect of a hole is to increase the separation (and amplitude) of some diffraction rings depending on the ratio between the diameters of the primary and secondary shadow. A new diffraction structure – diffraction spikes – appears for each vane inserted to hold the secondary, producing a six fold star pattern with the spider vane.

The procedure described above can be used to simulate a double star with different angular separations and magnitudes in order to analyze the effect of diffraction structures in the separation of the faint companion.

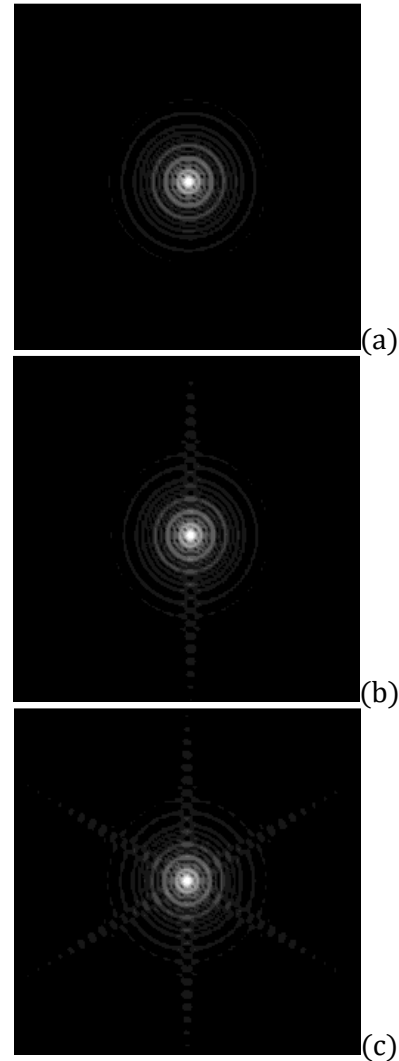


*Figure 4 Intensity plots representing star images for each of the telescope masks in Figure 2. (a) Circular hole; (b) Simple secondary holder; (c) spider vane. For each plot,  $\varepsilon=1$ . Other parameters are:  $L=1.4$ ,  $R_1=0.3$ ,  $R_2=0.045$ ,  $w=0.01$ , and  $l=0.5$ . The background factor was adjusted to enhance diffraction structures.*

### Simulating a binary star

To simulate a binary star using the diffraction integral of Eq. (1), one should regard each element as independent and non-coherent light sources. As such there is no interference between them, resulting in cancellation of the crossed terms in the Fresnel-Kirchhoff integral. In the scalar field approximation, there are no concerns about the polarization state of each source. Suppose then that we have a pair with intensities  $S_1$  and  $S_2$ . The final intensity can be represented using Eq. (10) with a displaced coordinate

Numerical Generation of Double Star Images for Different Types of Telescopes

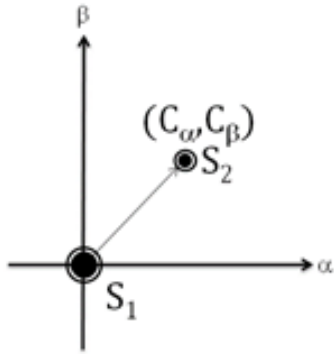


Figure 5: Coordinate position of a companion star in the  $(\alpha, \beta)$  plane.

$$I_{DS}(\alpha, \beta) = \log \left( |S_1(\alpha, \beta)|^2 + |S_2(\alpha + C_\alpha, \beta + C_\beta)|^2 + \varepsilon \right) \quad (11)$$

$(C_\alpha, C_\beta)$  for the companion

The apparent separation between each companion will be given simply by

$$\sqrt{C_\alpha^2 + C_\beta^2}$$

as represented by the vector from  $S_1$  to  $S_2$  in Figure 5. Since a straightforward map exists between the FFT output matrix, whose elements are labeled by a set of indexes  $(i, j)$ , and the angular apparent coordinates, the simulation of binaries with distinct separations is straightforwardly implemented by summing elements of two matrices with displaced elements. In matrix notation, Eq. (11) is written as

$$I_{DS}(i, j) = \log \left( |S_1(i, j)|^2 + |S_2(i + n, j + m)|^2 + \varepsilon \right) \quad (12)$$

where  $(n, m)$  are now the companion coordinates in displaced pixels or matrix indexes. Normalizing the primary star with unitary amplitude, one can take  $S_2 \rightarrow AS_1$  with  $0 < A \leq 1$ , so that the final binary amplitude model can be written as

$$I_{DS}(\alpha, \beta) = \log \left( |S(\alpha, \beta)|^2 + A^2 |S(\alpha + C_\alpha, \beta + C_\beta)|^2 + \varepsilon \right) \quad (13)$$

Therefore, the companion will be

$$\Delta m = 2.5 \log A^2 \quad (14)$$

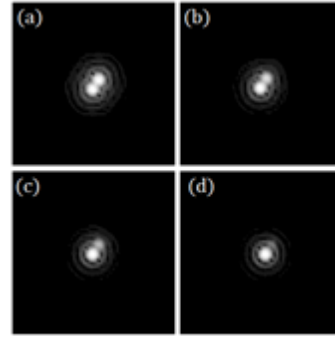


Figure 6 Simulation of a binary star with decreasing magnitude in a refractor telescope close to the Dawes' limit. (a)  $\Delta m=0$ ; (b)  $\Delta m=-1$ ; (c)  $\Delta m=-2$ ; (d)  $\Delta m=-4$ . Companion position in matrix notation is  $(n, m)=(2, 3)$ . Each frame has  $155 \times 155$  pixels.

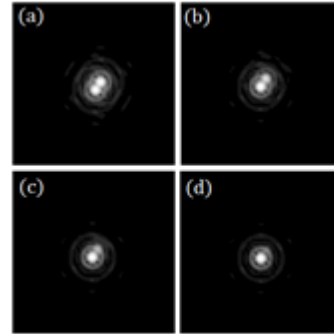


Figure 7. Simulation of a binary star with decreasing magnitude for the spider vane (close to the Dawes' limit). (a)  $\Delta m=0$ ; (b)  $\Delta m=-1$ ; (c)  $\Delta m=-2$ ; (d)  $\Delta m=-4$ . Companion position in matrix notation is  $(n, m)=(2, 3)$ . Each frame has  $155 \times 155$  pixels.

magnitudes below the primary according to this model (since  $A$  is less than one,  $\Delta m$  is negative).

As an initial test, we simulate the disappearance of a close companion in a refractor telescope as the companion magnitude is decreased (Figure 6). The secondary is close to the resolving power. The value of  $\varepsilon$  was increased to 40 to limit the number of visible diffraction rings. Other parameters used are:  $L = 1.4$ ,  $R_1=0.3$ . As a comparison, the case of the spider vane mask is shown in Figure 7. The reader may compare these simulations with Figure 3 in (Anton, 2015), for example.

It is evident from this initial numerical analysis that the companion fading depends on its position angle in relation to the diffraction spikes and not only on the main star apparent separation. At best (that is, in the case of no atmospheric turbulence) even when the companion is well separated in relation to the principal star, its observation is guaranteed provided there is

### Numerical Generation of Double Star Images for Different Types of Telescopes

some contrast between the companion and a diffraction feature. It was already remarked (Treanor, 1946) that the companion must fall on a minimum of a diffraction ring of the principal star and be brighter than the nearest secondary maxima in order to be visible. Such logical rule gives rise to a diagram on the magnitude-separation plane known as the *Peterson zone diagram* (Napier-Munn, 2008). Obviously, the companion limiting magnitude falls with increasing separation, since diffraction ring maxima decrease in magnitude with increasing separation of the main star. Let us then explore these relationships for more complex mask designs.

#### The Magnitude-Separation Diagram

In order to explore Peterson’s zone diagram for double stars, it is sufficient to find the zeros of the main star intensity function, which is proportional to  $|E(\alpha)|^2$  in Eq. (3) for the refractor case. Noting that  $\alpha \ll 1$ , we can write the image intensity function as  $\sim (J_1(\xi\alpha/\alpha^2))^2$  with  $\xi = kD/2$ . A straightforward derivation of the intensity function will give the first derivative  $h(\alpha)$  with

$$h(\alpha) = \xi\alpha J_0(\xi\alpha) - 2J_1(\xi\alpha) \tag{15}$$

where  $J_0$  is the zeroth order Bessel function (Abramowitz & Stegun, 1972). The roots of Eq. (15) can only be determined numerically and, for a 5 inch (127mm) refractor, some of the roots are shown in Table 1, together with the diffraction ring maximum values  $\Delta m$  (above the main star magnitude) normalized for a zero magnitude star.

The last root (called “inf” in Table 1) corresponds to a separation of  $\sim 15.5''$  where the theoretical zero meets the telescope limiting magnitude. This value was calculated as  $\sim 11.8$  assuming an adapted eye’s pupil of 7 mm and unassisted limiting magnitude of 5.5.

According to this numerical modeling, the “main star effective radius” of a 5 inch refractor is about 16 seconds of arc. Using again a 5 inch refractor as an example, Figure 8 shows the Airy function on a magnitude-separation graph. Three regimes of distance can be seen: (i) the “hard wall” limiting separation below 1” (Dawes’ limit); (ii) from  $\sim 1''$  to  $16''$ , a linear increase in the magnitude difference (noting that the separation is in log scale) and (iii) above  $16''$ , with the existence of a flat region imposed by the sky background.

A direct comparison between a 5-inch and a 10-inch telescope on an “undisturbed” magnitude separation diagram is seen in Figure 9.

Table 1. Some zeros of Eq. (15) in seconds of arc and maximum values of magnitude differences for a 5 inch refractor.

| Zero | Separation | Max. Value |
|------|------------|------------|
| 1    | 1.15133    | 4.33925    |
| 2    | 2.4803     | 5.9527     |
| 3    | 3.4241     | 6.9892     |
| 4    | 4.3600     | 7.7705     |
| 5    | 5.2923     | 8.3987     |
| inf  | 15.4959    | 11.8924    |

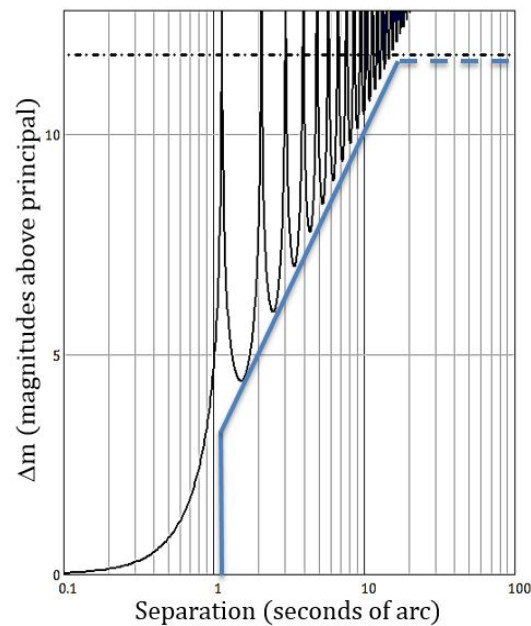


Figure 8 – Plot of a star intensity function (profile of Airy function) normalized to zero magnitude central star for a 5 inches refractor telescope.

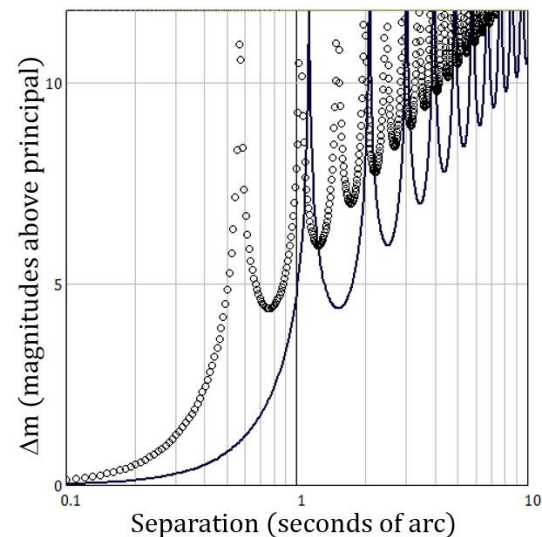


Figure 9. Theoretical magnitude separation plot (normalized for zero at the main star) for a 5-inch (line) and 10-inch refractor telescope (circles).

Numerical Generation of Double Star Images for Different Types of Telescopes

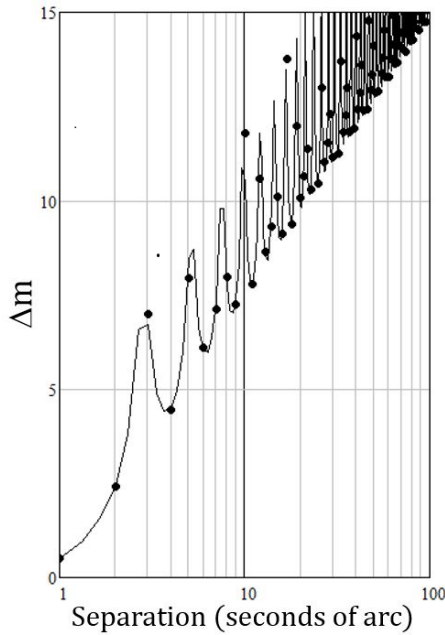


Figure 10 Comparison between the exact formula (line) and the FFT calculation (circles) for a 2-inch circular aperture (refractor case). 4096 x 4096 points were used to generate the pattern.

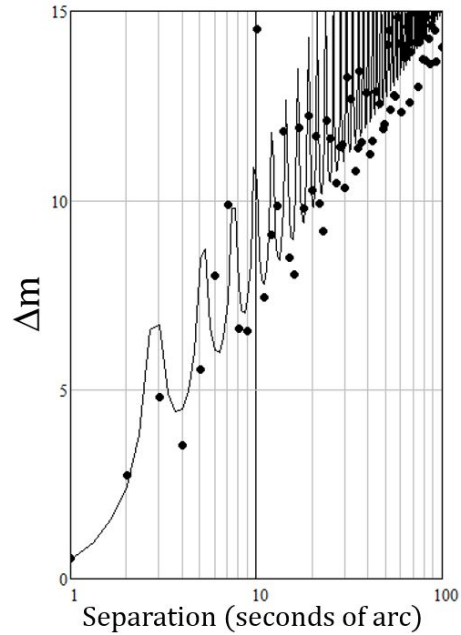


Figure 11. Effect of a hole mask (circles) with  $e=0.27$  (same case as Figure 10) compared to the unobstructed aperture or refractor (line).

**Numerical Evaluation of New Limiting Magnitudes Due to Mask Presence**

We numerically evaluate the limiting magnitude shift ( $\delta m$ ) in the diffraction pattern due to the presence of a complex mask. As we have seen, the mask contributes to make the diffraction pattern sharper than the unobstructed case, thus reducing the separation power as a function of the companion magnitude. Unfortunately, it is not possible to find any brightness formula for a given mask and therefore numerical evaluation is mandatory. First, we calibrate the FFT process with the exact formula of normalized magnitude as calculated by the amplitude field of Eq. (3). Due to limitations in computer memory, we restrict the FFT grid to 4096 X 4096 elements (corresponding to a  $2^n \times 2^n$  matrix with  $n = 12$ ) and solve the patterns for a 2 inch aperture diameter refractor. The good fit between the normalized magnitude as calculated by the exact formula (Eq. 3) and the numerical version is seen in Figure 10. Now the first diffraction ring is  $\sim 4''$  away from the main star.

Once the model is calibrated, the masks are applied. Figure 11 is the normalized magnitude separation diagram for a circular hole mask with  $e=0.27$  (ratio between hole and aperture diameters). At the first ring (separation radius  $4''$ ), the estimated magnitude difference is  $\delta m = -0.9674$ . As shown in Figure 11, the minima of the hole mask follow a straight envelop

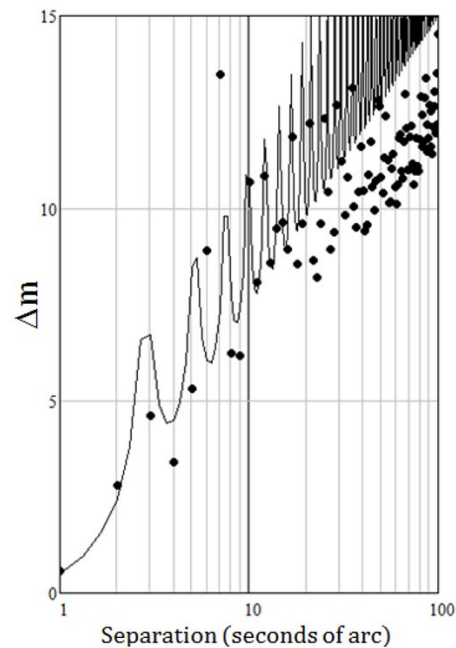


Figure 12. Effect of a circular hole mask (circles) and single holder vane (case of Figure 2b) with  $e=0.27$  compared to the unobstructed aperture (refractor), again for a 2 inch aperture. The pattern orientation is exactly aligned with the vane holder.  $R_1 = 0.3$ ,  $e=0.27$ ,  $w = 0.01$  and  $l = 0.5$ , see Eq. (7) and (8) for the meaning of each parameter.

which is about one magnitude below (therefore the diffraction pattern is one magnitude brighter than) the unobstructed case. Another interesting case is the sin-

### Numerical Generation of Double Star Images for Different Types of Telescopes

gle vane with obstruction as shown in Figure 2(b). The corresponding pattern is in Figure 4(b) and here the *orientation of the companion* (angle between the a-axis and  $S_1S_2$  in Figure 5) should be considered. If the companion orientation does not fall on the holder diffracting spikes, the corresponding magnitude separation diagram is much like the one of Figure 11. However, if there is perfect alignment, then a new plot emerges as shown in Figure 12. Now the magnitude difference for the low order rings follows the same values of the simple hole case (that is, there is minimal influence of the vane holder). However, as the separation from the principal increases, the vane holder decreases the companion contrast so that  $\delta m \leq -2$  for separations that are larger than 20".

Finally, as an evolution of secondary vane types, the circular holder (Figure 13) promises to reduce the effect of diffraction spikes caused by straight holders. To analyze this case, we rewrite the circular vane function as

$$H_{circular}(u,v) = H_{hole}(u,v) \Theta \left[ \sqrt{(v-C_0)^2 - u^2} - R_{ext} \right] \Theta \left[ \frac{R_{int}}{\sqrt{(v-C_0)^2 - u^2}} \right], \tag{16}$$

with  $R_{ext}$  and  $R_{int}$  external and internal vane radius and  $C_0$  the coordinate of the holder center (along the  $v$  axis).

As shown in Figure 14, most of the diffraction residue is due to the central hole. A comparison with Figure 12 shows a reduction in the secondary maxima for distances larger than 30" from the principal. In this sense, the circular vane performance is between the cases of (Figure 11) and (Figure 12).

#### Final remarks

By discussing diffraction patterns of several telescope masks, this article justifies the reason to choose refractor telescopes as ideal instruments in double star observation. This reason is not purely linked to the optical excellence of many instruments, but fundamentally related to the aperture geometry. The results above are strongly influenced by the presence of turbulence when we compare them to the star appearance at the telescope eyepiece. The effect of atmospheric blurring further limits the resolving power and observation efficiency of most telescopes, mainly if the task is to separate close binaries with distinct magnitudes because the star brightness gets mixed with the diffraction features. As is well known, as the telescope

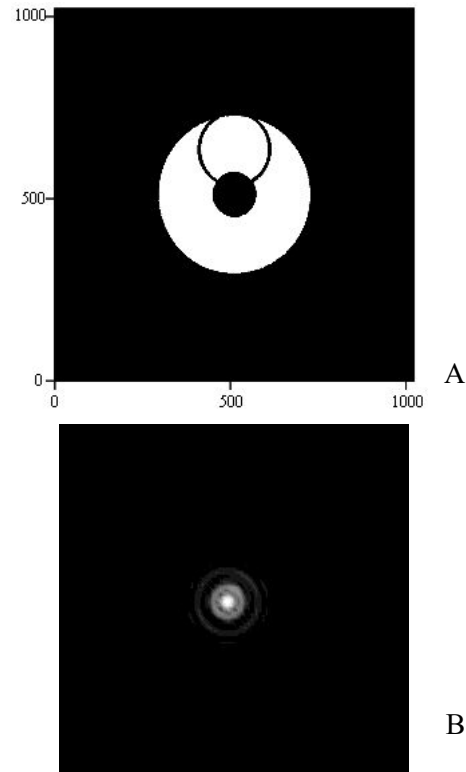


Figure 13. (A) Circular vane (Eq. 16) with  $R_i=0.3$ ,  $e=0.27$ ,  $L = 0.7$ ,  $R_{ext}=0.140$ ,  $R_{int}=0.135$  and  $C_0=0.17$ ; (B) Simulated stellar image.

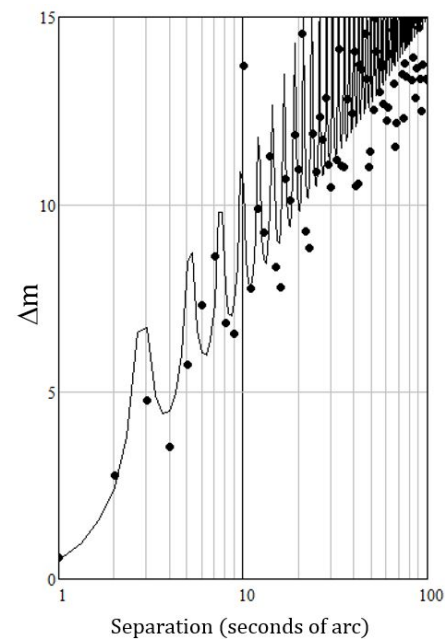


Figure 14. Effect of a circular vane (Figure 13b) with  $\epsilon=0.27$  compared to the unobstructed aperture (refractor), again for a 2 inch telescope

## Numerical Generation of Double Star Images for Different Types of Telescopes

size increases, the diffraction rings (and the star's apparent diameter) decrease, however, the atmospheric turbulence is aggravated by the increased size of the incident wave front, which becomes more sensible to variations in the air density and temperature.

In this work, we review the diffraction theory used to obtain a stellar image as the two-dimensional Fourier transformation of the instrument mask in the so-called "scalar approximation" of a propagation phenomenon of vector fields. Some details about how to obtain images were discussed together with a straightforward application to double stars. The details involve the choice of suitable mask functions for several types of secondary vanes as commonly found in most amateur telescopes. The mask is Fourier transformed and a suitable calibration is used to provide the scale for the magnitude-separation diagram which can then be theoretically calculated. In a special case, although circular secondary vanes are recommended to mitigate the diffraction spikes of straight holders, the effect is not as pronounced as would be expected based on intuition alone. The procedure described here can be adjusted to simulate the diffraction pattern of any type of mask for any telescope size.

### References

- Abramowitz, M. and Stegun, I., *Handbook of Mathematical Functions with Formulas, Graphs, and Mathematical Tables*, New York, Dover, 1971.
- Airy, G. B., 1835, "On the Diffraction of an Object-glass with Circular Aperture", *Transactions of the Cambridge Philosophical Society*, vol. 5, Pt.III, XII.
- Anton, R., 2015, "Double Star Measurements at the Southern Sky with a 50 cm Reflector and a Fast CCD Camera in 2014", *Journal of Double Star Observation*, **11**(2), 81-90.
- Argyle, B., *Observing and Measuring Visual Double Stars*. Springer, 2004.
- Barten, P., *Contrast Sensitivity of the Human Eye and Its Effects on Image Quality*. SPIE Optical Engineering Press, 1999.
- Berrevoets, C., 2001, *Aberrator*. Version 3, update 2. Available at <http://aberrator.astronomy.net/>.
- Cooley, J., Lewis, P., & Welch, P., 1967, "History of the fast Fourier transform", In Proc. IEEE, **55**, 1675-1677.
- Dawes, W. R., 1865, Memoirs of the Royal Astronomical Society, **35**, p.154.
- Klein, M. V., *Optics*. John Wiley & Sons, 1970.
- Labeyrie, A., 1970, "Attainment of Diffraction Limited Resolution in Large Telescopes by Fourier Analysing Speckle Patterns in Star Images", *Astronomy and Astrophysics*, **6**, 85-87.
- Napier-Munn, T., 2008, "A Mathematical Model to Predict the Resolution of Double Stars by Amateur and Their Telescopes", *Journal of Double Star Observations*, **4**, 156-163.
- PTC, 2010, *Mathcad 15.0 User's Guide*. Parametric Technology Corporation.
- Schroeder, D. J., 1987, *Astronomical Optics*. Academic Press.
- Stoltzmann, D. E., 1983, "The perfect point spread function", *Applied Optics and Optical Engineering*, **9**, 111-148.
- Treanor, B., 1946, "On the Telescopic resolution of unequal binaries", *The Observatory*, **66**, 255-258.

